

RESEARCH ARTICLE | NOVEMBER 19 2024

Automated potential energy surface development and quasi-classical dynamics for the $F^- + SiH_3I$ system **FREE**

Balázs J. Molnár ; Attila Á. Dékány ; Gábor Czakó  



J. Chem. Phys. 161, 194306 (2024)

<https://doi.org/10.1063/5.0238366>



Articles You May Be Interested In

KoopmanLab: Machine learning for solving complex physics equations

APL Mach. Learn. (September 2023)

Experimental realization of a quantum classification: Bell state measurement via machine learning

APL Mach. Learn. (September 2023)



The Journal of Chemical Physics

Special Topics Open for Submissions

[Learn More](#)

Automated potential energy surface development and quasi-classical dynamics for the $F^- + SiH_3I$ system

Cite as: J. Chem. Phys. 161, 194306 (2024); doi: 10.1063/5.0238366

Submitted: 11 September 2024 • Accepted: 31 October 2024 •

Published Online: 19 November 2024



View Online



Export Citation



CrossMark

Balázs J. Molnár,  Attila Á. Dékány,  and Gábor Czako^{a)} 

AFFILIATIONS

MTA-SZTE Lendület “Momentum” Computational Reaction Dynamics Research Group, Interdisciplinary Excellence Centre and Department of Physical Chemistry and Materials Science, Institute of Chemistry, University of Szeged, Rerrich Béla tér 1, Szeged H-6720, Hungary

^{a)} Author to whom correspondence should be addressed: gczako@chem.u-szeged.hu

ABSTRACT

We report a potential energy surface (PES) development for the $F^- + SiH_3I$ system to study its gas-phase reactions through quasi-classical dynamics simulations. The PES is represented by a full-dimensional permutationally invariant polynomial fitted to composite coupled cluster energy points obtained at the ManyHF-[CCSD-F12b + BCCD(T) – BCCD]/aug-cc-pVTZ(-PP) level of theory. The development was automated by ROBOSURFER, which samples the configurational space, manages *ab initio* calculations, and iteratively extends the fitting set. When selecting the *ab initio* method, we address two types of electronic structure calculation issues: first, the gold standard CCSD(T)-F12b is prone to occasional breakdown due to the perturbative (T) contribution, whereas CCSD-F12b + BCCD(T) – BCCD, with the Brueckner (T) term, is more robust; second, the underlying Hartree–Fock calculation may not always converge to the global minimum, resulting in highly erroneous energies. To mitigate this, we employed ManyHF, configuring the Hartree–Fock calculations with multiple initial guess orbitals and selecting the solution with the lowest energy. According to the simulations, the title system exhibits exceptionally high and diverse reactivity. We observe two dominant product formations: S_N2 and proton abstraction. Moreover, $SiH_2F^- + HI$, $SiHFI^- + H_2$, $SiH_2FI + H^-$, $SiH_2 + FHI^-$, $SiH_2 + HF + I^-$, and $SiHF + H_2 + I^-$ formations are found at lower probabilities. We differentiated inversion and retention for S_N2 , both being significant throughout the entire collision energy range. Opacity- and excitation functions are reported, and the details of the atomistic dynamics are visually examined via trajectory animations.

Published under an exclusive license by AIP Publishing. <https://doi.org/10.1063/5.0238366>

I. INTRODUCTION

Since silicon (Si) is below carbon (C) in the periodic table, one may expect similar chemistry of systems with C and Si centers. However, as several electronic structure studies showed, there are notable differences between the valence-isoelectronic C- and Si-centered systems.^{1–10} For example, the $[X\cdots CH_3\cdots Y]^-$ structure corresponds to a transition state (TS) of the $X^- + CH_3Y$ [$X, Y = F, Cl, Br, I, \text{etc.}$] bimolecular nucleophilic substitution (S_N2) reactions, whereas $[X\cdots SiH_3\cdots Y]^-$ is a relatively stable complex, i.e., a minimum on the potential energy surface (PES) of the $X^- + SiH_3Y$ system.^{1–10} Furthermore, in the case of $[X\cdots CH_3\cdots Y]^-$, a collinear (or nearly collinear if X and/or Y are complex ligands) TS is clearly preferred,^{5,6,10,11} which plays a key role in the

Walden-inversion mechanism of the corresponding S_N2 reaction. In the case of $[X\cdots SiH_3\cdots Y]^-$, the collinear and bent structures have similar energies, thereby opening a real competition between the Walden-inversion and front-side attack pathways of the $X^- + SiH_3Y$ S_N2 reactions.^{5,10} Unlike at silicon centers, the dynamics of S_N2 reactions at carbon centers have been widely studied;^{12–41} however, the above-mentioned interesting properties motivate us to investigate the atomic-level dynamics of the Si-centered reactions as well. As the SiH_3Y systems are hard to handle experimentally, performing first-principles theoretical simulations seems to be the best way to proceed toward providing new insights into the mechanisms of the $X^- + SiH_3Y$ reactions. Recently, we carried out such simulations for the $F^- + SiH_3Cl$ reaction,^{42,43} and here we plan to report a similar study for the $F^- + SiH_3I$ system. With the new results at hand, we

can investigate the leaving group effects in Si-centered reactions, and we can also study the central atom effect by comparing the present results with those obtained for the $F^- + CH_3I$ reaction.²⁴

We use the ROBOSURFER program package⁴⁴ to construct an analytical *ab initio* PES for the title reaction by fitting high-level *ab initio* energy points, which surface can be utilized in quasi-classical trajectory (QCT) simulations. During the PES development, a large configuration space needs to be sampled because of the relatively easy cleavage of the Si–H and Si–I bonds, resulting in multiple chemically relevant two- and three-fragment channels of the $F^- + SiH_3I$ reaction. Since the fitting set contains many geometries far from the stationary-point regions, one may expect *ab initio* issues, such as Hartree–Fock convergence problems⁴⁵ and/or the breakdown of the perturbative (T) approximation,⁴⁶ which may result in erratic energies causing a large number of unphysical trajectories. In the present work, we demonstrate how to solve these issues using robust electronic structure techniques.^{45,46}

In Sec. II, we describe the methods and computational details, focusing on the automated iterative PES development. In Sec. III, we report the properties and accuracy of the PES and discuss the results of the dynamics simulations, revealing the reactivity and atomic-level mechanisms of the various product channels of the title reaction. The paper ends with a summary and conclusions in Sec. IV.

II. METHODS AND COMPUTATIONAL DETAILS

A. Constructing the initial fitting set

The initial fitting set of the $SiH_3I + F^-$ system is constructed from randomly displaced versions of eight stationary points (minima: WMIN, FSPostMIN, *syn*- and *anti*-FBHMIN, *syn*-IBHMIN and IDHBMIN, transition states: FDITS and IDITS), the reactants ($SiH_3I + F^-$), six products with two fragments ($SiH_3F + I^-$, $SiH_2I^- + HF$, $SiH_2F^- + HI$, $SiHFI^- + H_2$, $SiH_2FI + H^-$, and $SiH_2 + FHI^-$), and six products consisting of three fragments ($SiH_2 + HI + F^-$, $SiH_2 + HF + I^-$, $SiHF + HI + H^-$, $SiHF + H_2 + I^-$, $SiHI + HF + H^-$, and $SiHI + H_2 + F^-$). Some of the stationary points (WMIN, FSPostMIN, FDITS, IDITS) were previously reported by our research group.¹⁰ (See Sec. III A for the notations.) In the geometry optimizations, we employed an explicitly-correlated coupled-cluster singles, doubles, and perturbative triples method, CCSD(T)-F12b.⁴⁷ For the lighter atoms, such as hydrogen, fluorine, and silicon, we utilized the augmented correlation-consistent triple-zeta basis set aug-cc-pVTZ.⁴⁸ For the heavy iodine atom, we considered relativistic effects by using a relativistic effective core potential along with the aug-cc-pVTZ-PP basis set.⁴⁹ Throughout the article, we refer to this combination as AVTZ(-PP).

The Cartesian coordinates of the stationary points in the interaction region were randomly displaced within the 0–0.32 Å interval, and the polyatomic fragments of both the reactants and the products were randomly rotated with respect to each other, maintaining their center of mass distance between 1.5 and 15 Å. Subsequently, we randomly displaced their geometries in the 0–0.32 Å interval as well. For each optimized structure, 500 perturbed geometries were generated for a total of 10 500. The *ab initio* energies of these structures were obtained by a composite coupled cluster method with a combination of CCSD-F12b and the Brueckner coupled cluster⁵⁰ perturbative triples, BCCD(T), with the AVTZ(-PP) basis set,

$$E_{\text{composite}} = [\text{CCSD-F12b} + \text{BCCD(T)} - \text{BCCD}]/\text{aug-cc-pVTZ(-PP)}. \quad (1)$$

The justification behind utilizing this composite method instead of the more traditional CCSD(T)-F12b for computing the energies of the fitting set is that in our previous study, we observed that the perturbative (T) contribution is prone to occasional breakdown. This issue can largely be circumvented with the above composite method.⁴⁶ We utilized the MOLPRO 2015.1 program package for performing geometry optimizations, single-point calculations, and developing the potential energy surface.⁵¹ Due to electronic structure calculation problems, some of the energy computations failed, and points with too high energies were rejected; therefore, the initial fitting set contained 10 325 points.

B. Potential energy surface fitting

Here, we define the PES as a full-dimensional polynomial of Morse variables, up to a degree D . This polynomial is invariant to permutations of like-atoms,^{52–54} and its coefficients are determined through a weighted least-squares (WLS) fit to *ab initio* energy points.

In our context, a full-dimensional PES is a function of all possible interatomic distances, a total of $N(N-1)/2$ for a chemical system of N atoms, which is 15 in the case of $SiH_3I + F^-$. We note that the number of internal coordinates needed to define a geometry is (much) smaller if N is greater than four. Nevertheless, we must utilize the full set of interatomic distances because they form a closed group for permutation.

Morse variables, denoted as y_{ij} , represent exponentially transformed r_{ij} interatomic distances, where $y_{ij} = e^{-r_{ij}/a}$, with a being the damping parameter controlling the asymptotic behavior of the energy surface. For the title system, the chosen value for the damping parameter is 3 bohrs, based on our previous experience with ion–molecule collisions.^{20,24}

During the PES development, we used fifth- and sixth-order polynomial bases depending on the size of the fitting set, the expansion of which contains 3292 and 10 810 coefficients. It is important that the useful solution of the fitting problem necessitates an overdetermined system of equations, meaning that the size of the fitting set must always exceed the number of coefficients. The details of the energy surface fitting via WLS are described in our previous article.⁴²

For the WLS, two different weight functions were utilized that computed weights ranging between zero and one depending on the relative energy, as illustrated in Fig. 1,

$$w_a(E_{\text{rel}}) = \frac{E_a}{E_{\text{rel}} + E_a - E_{\text{min}}} \frac{E_b}{E_{\text{rel}} + E_b - E_{\text{min}}}. \quad (2)$$

Equation (2) represents a simpler asymptotically decaying weight function in which parameters E_a and E_b were set to 94.1 and 313.8 kcal/mol, and the E_{rel} relative energies were defined as relative to the free reactants. E_{min} denotes the relative energy of the global minimum, WMIN, at –82.3 kcal/mol.

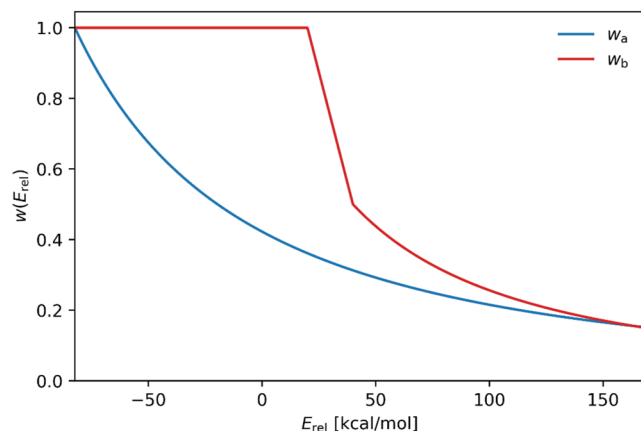


FIG. 1. Weight functions used in the WLS fitting: w_a is a one-stage function with asymptotic decay, and w_b is a three-stage function with constant, linear decay, and asymptotic decay regions. E_{rel} is relative to the energy of the reactants.

Equation (3) defines a more sophisticated three-stage weight function, w_b , in which the parameters E_a , E_b , E_c , E_d , and f were set to 94.1, 313.8, 20, 40 kcal/mol, and 0.5, respectively,

$$w_b(E_{\text{rel}}) = \begin{cases} f \frac{E_a}{E_{\text{rel}} + E_a - E_d} \frac{E_b}{E_{\text{rel}} + E_b - E_d} & \text{if } E_{\text{rel}} > E_d, \\ 1 + \frac{f-1}{E_d - E_c} (E_{\text{rel}} - E_c) & \text{if } E_c < E_{\text{rel}} \leq E_d, \\ 1 & \text{if } E_{\text{rel}} \leq E_c. \end{cases} \quad (3)$$

The first stage of w_b is constant 1 for the deepest energies all the way up to E_c , which is the starting point of the linear decay. E_d represents the end of the linear part and the start of the asymptotically decaying section with an initial weight of f . As Fig. 1 shows, the w_a weight function reduces the contributions of the fitting points in a significant part of the chemically relevant energy range, while w_b assigns a constant weight all the way up to 20 kcal/mol.

C. Potential energy surface development

For the potential energy surface development, we employed the ROBOSURFER program system, which iteratively improves the fitting set by extending it with carefully selected energy points.⁴⁴ In each iteration, 987 simulations were conducted within the impact parameter range of 0–10 bohrs using a step size of 0.5 bohr at a fixed collision energy. To assess the quality of the potential energy surface, we monitored both the percentage of the unphysical trajectories and the root-mean-square errors (RMSEs) of the energies of the fitting set in the chemically relevant energy regions. These regions were defined as below 20 kcal/mol and between 20 and 40 kcal/mol relative to the energy of the free reactants, in accordance with the energy ranges of the constant and the linearly decreasing sections of the w_b weight function applied in the fitting. The *ab initio* energies were obtained as $E_{\text{composite}}$ [Eq. (1)] all the way up to the 376th PES iteration and as

$$E_{\text{ManyHF}} = \text{ManyHF} - [\text{CCSD-F12b} + \text{BCCD(T)} - \text{BCCD}] / \text{aug-cc-pVTZ(-PP)}, \quad (4)$$

for subsequent iterations. The prerequisite for the reliability of high-level *ab initio* calculations is that the underlying Hartree–Fock energy is the global minimum solution. The ManyHF method,⁴⁵ developed by our research group, aims to minimize the likelihood of yielding extremely erroneous energies originating from Hartree–Fock convergence issues. We note that for most of the calculations, the $E_{\text{composite}}$ and E_{ManyHF} energies are equal.^{45,55}

The evolution of the quality of the PES and the size of the fitting set during the development as a function of ROBOSURFER iteration are shown in Fig. 2. A trajectory was considered unphysical if it terminated in a geometry with more than three fragments. The determination of the connectivity of the chemical structures was based on interatomic distances: two atoms are considered adjacent if their spatial distance is smaller than the sum of their corresponding covalent radii plus a constant distance, 0.8 Å. The covalent radii of hydrogen, fluorine, and iodine were defined as 0.31, 0.57, and 1.39 Å, respectively.⁵⁶ The radius of silicon was set to 1.60 Å, following our previous study on the $\text{F}^- + \text{SiH}_3\text{Cl}$ system.⁴²

The development process started at a collision energy of 1 kcal/mol, which was increased to 10 kcal/mol as the ratio of the unphysical trajectories reduced below 1%. Subsequent simulations were run up to 80 kcal/mol collision energy with a step size of 10 kcal/mol. Starting from the initial fitting set, we conducted the development through 195 iterations. During this period, the fitting errors sharply increased and approached 1.4 and 2.8 kcal/mol in the lower and higher energy regions. Simultaneously, the size of the fitting set reached 13 490 points, providing the opportunity for applying sixth-order fitting between PES iterations 196 and 376.

As shown by Fig. 2, when transitioning to the sixth-order fitting, nearly all trajectories were unphysical initially, but their percentage rapidly decreases as the development progresses. The collision energy of 1 kcal/mol was employed up to the 356th PES iteration. After that, we increased the collision energy according to the previously described strategy. Simultaneously, the RMSEs increased modestly, starting from 0.1 kcal/mol at PES196 and reaching 0.7 and 1.3 kcal/mol in the lower and higher PES regions at PES376. For the fitting, we used the w_a weight function, defined by Eq. (2), up to the 376th PES iteration.

From the multitude of simulations run on PES376, we selected 32 trajectories to represent the most significant mechanisms leading to the formation of the two-fragment products. To further test the PES, we calculated the energies of the geometries along these representative trajectories using the composite coupled cluster method defined by Eq. (1). The root-mean-square error between *ab initio* and PES376 energies exceeded 10 kcal/mol for most of the trajectories, necessitating further improvement of the PES.

During the development, we identified two new stationary points (FSMIN and FDHBMIN) and a new product channel ($\text{SiH}_3 + \text{FI}^-$). We optimized and perturbed their geometries as described before, resulting in a total of 1500 geometries. The energies of these points were calculated using the composite coupled cluster method. However, most of the computations for the $\text{SiH}_3 + \text{FI}^-$ geometries did not converge; therefore, we were only able to add 1041 points to the fitting set manually.

Starting from PES377, we used a different weight function for the fitting, as defined by Eq. (3). This adjustment was motivated by the previous weight function, which significantly devalued chemically relevant points with higher energy, leading to their

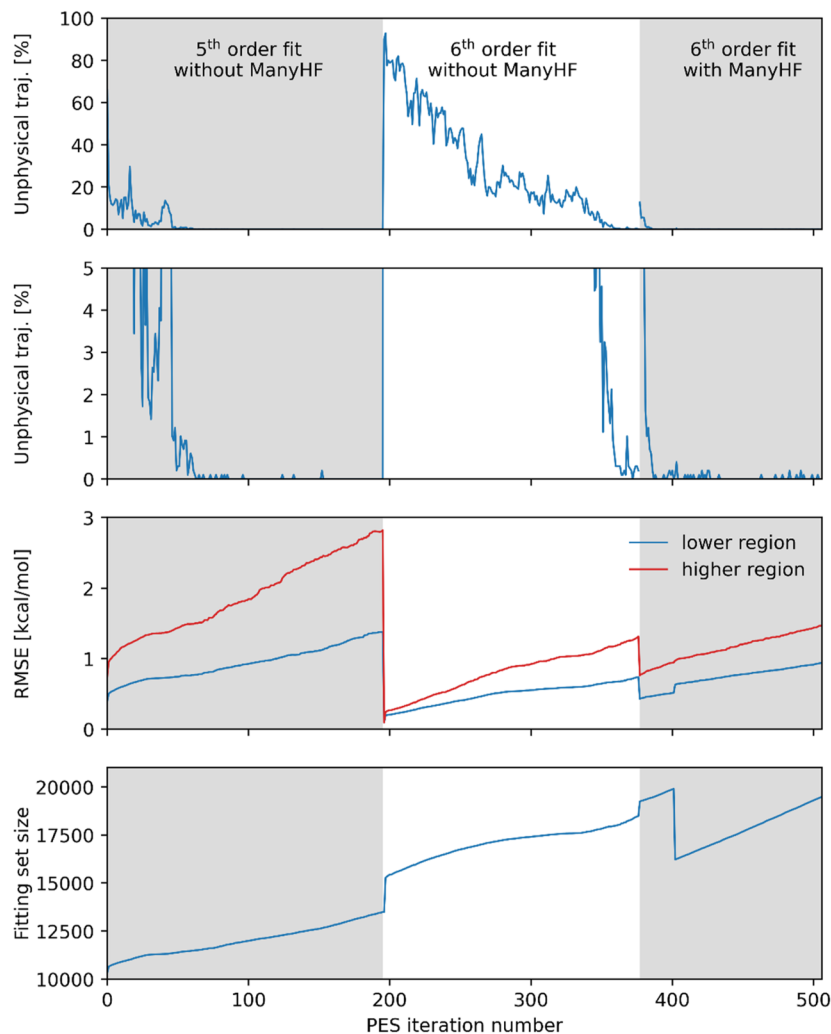


FIG. 2. Evolution of different properties of the PES during the development: the percentage of the unphysical trajectories (upper two panels with different ordinate ranges); the root-mean-square fitting errors in the lower and higher segments of the chemically relevant region (third panel); and the size of the fitting set (bottom panel) as functions of the PES iterations. The lower and higher segments of the chemically relevant region are defined as -82.3 – 20 and 20 – 40 kcal/mol relative to the reactants.

disproportionately low contributions to the fitting. The last part of the development was the re-selection of the fitting set, during which we removed points from the unnecessarily overrepresented regions of the PES and then further expanded the re-selected set with ROBOSURFER until the quality of the energy surface became sufficient. We finished the development at PES506, consisting of 19 492 energy points.

D. Quasi-classical trajectory simulations

We conducted quasi-classical trajectory simulations at 13 different collision energies (1, 5, 10, 15, 20, 25, 30, 35, 40, 50, 60, 70, and 80 kcal/mol) utilizing the final potential energy surface, PES506, and our own QCT code. Impact parameters were set within the range from 0 to b_{\max} , with a step size of 0.5 bohr. Here, b_{\max} represents the smallest impact parameter where only nonreactive collisions were observed. The values of b_{\max} for the collision energies arranged in increasing order are as follows: 26.5, 19.5, 16, 15, 14, 13.5, 13, 12.5,

12, 11.5, 11, 11, and 11 bohrs. A total of 5000 simulations were executed at each impact parameter and collision energy, resulting in 1 930 000 trajectories.

In the initial state of the simulations, we set the vibrational energy of SiH_3I to its zero-point energy, and we set its rotational energy to 0 using normal mode sampling.⁵⁷ We randomly rotated the polyatomic reactant, and the initial center-of-mass distance was defined by the expression $\sqrt{x^2 + b^2}$, where the parameter x was 40 bohrs at 1 kcal/mol and 25 bohrs at higher collision energies. The trajectories were propagated with a $3\hbar/E_h$ time step utilizing the velocity Verlet algorithm.^{58,59} The simulations were terminated when the longest interatomic distance became at least 1 bohr greater than the initial maximum atom-atom distance.

We applied two harmonic zero-point energy constraints: soft and hard. If the sum of the vibrational energies of the product fragments reached the sum of their harmonic zero-point energies, then it satisfies the soft vibrational constraint. The hard vibrational constraint necessitates that all product fragments possess

a vibrational energy equal to or greater than their zero-point energy.

We identified the products based on the connectivity of the final trajectory step. In our methodology, a product is considered successfully identified if its adjacency list can be found in the permutationally invariant set of the adjacency lists of the corresponding reference structure. In the case of vibrationally highly excited products, it is possible that the terminating trajectory step is so distorted that its momentary connectivity differs from all references, resulting in an unidentified product.⁴²

In the case of two co-products, moving in opposite directions and being at a significant distance from each other at the terminating step guarantees that their interaction will only decrease if the simulation continues. However, for three-fragment products, we can only ensure that at least one product fragment is sufficiently separated from the others. If the other two fragments are interacting, it is possible that the simulation was terminated before the final step of a compound multistep reaction mechanism.

To minimize the number of trajectories resulting in misidentified and unidentified products, we further propagated the problematic trajectories for a few thousand extra steps and replaced the final step of these simulations if a better replacement was found along the further propagated trajectory; otherwise, we kept the original. In the

case of three-fragment product geometries, a better trajectory step is the first trajectory step resulting in two fragments, and in the case of an unidentified structure, a better replacement means the first identifiable structure. If an initially unidentifiable product is followed by an identifiable three- and then a two-fragment geometry, the first two-fragment structure is chosen.

For the differentiation of inversion and retention iodide ion substitution products, we used a vector projection method that was developed in our research group and utilized in the stereochemical analysis of multiple S_N2 reactions.^{42,60–64}

The trajectories were analyzed by our own Python package, which is available in Ref. 65 with documentation in Ref. 66.

III. RESULTS AND DISCUSSION

A. Schematic potential energy surface

Figure 3 shows the transition states, minima, and the different reaction channels of $\text{SiH}_3\text{I} + \text{F}^-$ and the relative energies calculated at $E_{\text{composite}}$, which are in this case equal to E_{ManyHF} , as well as obtained on PES506. This schematic energy surface predicts an unusually complex reaction profile for a chemical system of this small size, which is worth comparing to two analogous systems,

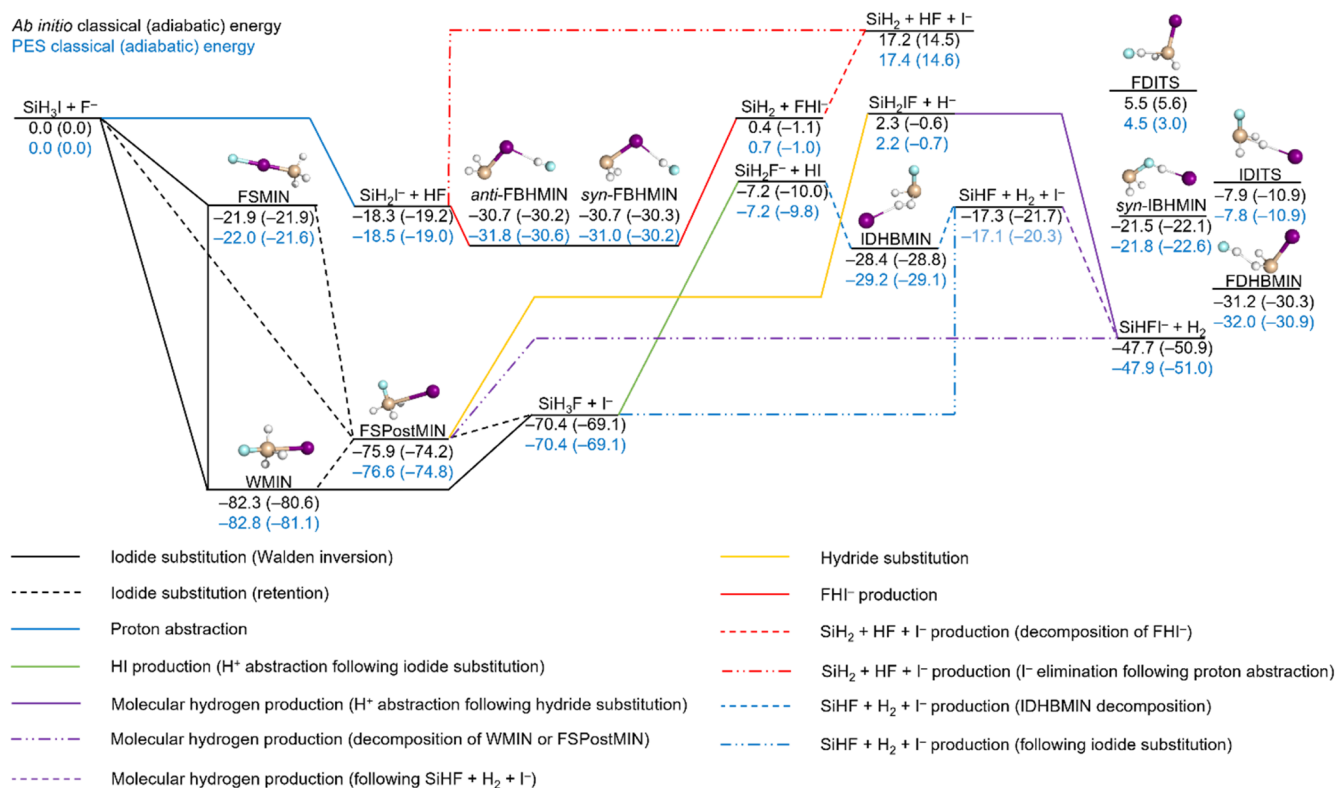


FIG. 3. Schematic PES of the $\text{SiH}_3\text{I} + \text{F}^-$ system, with structures of the stationary points and relative energies in kcal/mol. The classical *ab initio* energies are computed at the [CCSD-F12b + BCCD(T) – BCCD]/AVTZ(-PP) level of theory, and the harmonic zero-point vibrational corrections of the adiabatic energies are obtained at CCSD(T)-F12b/AVTZ(-PP).

$\text{SiH}_3\text{Cl} + \text{F}^-$ and $\text{CH}_3\text{I} + \text{F}^-$. With the former, we can examine the effect of replacing the substituent with a different halogen, and with the latter, the central atom effect can be studied.

The most exothermic reaction in the title system is the iodide ion substitution [$\Delta E_e(\Delta H_0) = -70.4(-69.1)$ kcal/mol], producing $\text{SiH}_3\text{F} + \text{I}^-$ via two barrierless mechanisms: the Walden inversion characterized by the global minimum WMIN complex at $-82.8(-81.1)$ kcal/mol, typical of back-side attack, and the retention channel with another deep negative-energy minimum, FSPostMIN at $-76.6(-74.8)$ kcal/mol, associated with front-side attack. A front-side attack might also result in FSMIN formation at $-22.0(-21.6)$ kcal/mol, which is a complex featuring an F-I bond. Such interhalogen interaction is characteristic to the $\text{CH}_3\text{I} + \text{F}^-$ system as well, exerting a great influence on the dynamics, but the analogous structure with the F-Cl bond, $[\text{SiH}_3-\text{Cl}\cdots\text{F}]^-$, is lacking in $\text{SiH}_3\text{Cl} + \text{F}^-$. Considering the energetics of FSPostMIN and WMIN, a mixture of inversion and retention products can be expected even at the lowest collision energies, similarly to the $\text{SiH}_3\text{Cl} + \text{F}^-$ system and in contrast to $\text{CH}_3\text{I} + \text{F}^-$, where the retention is characteristic of higher collision energies via the front-side attack mechanism and with double inversion at moderately high collision energy.

The WMIN and FSPostMIN complexes can decompose via hydride ion substitution, resulting in $\text{SiH}_2\text{FI} + \text{H}^-$ [$\Delta E_e(\Delta H_0) = 2.2(-0.7)$ kcal/mol]. An athermic hydride ion substitution is observed in the case of $\text{SiH}_3\text{Cl} + \text{F}^-$, and for the $\text{CH}_3\text{I} + \text{F}^-$ PES, the analogous reaction is highly endothermic and opens above 50 kcal/mol.¹⁰

The $\text{SiH}_3\text{I} + \text{F}^-$ PES features a proton-abstraction channel [$\Delta E_e(\Delta H_0) = -18.5(-19.0)$ kcal/mol], which due to its simple, direct mechanism and exothermicity is expected to be one of the most dominant product formations in this system. *Syn*- and *anti*-FBHMIN complexes can follow proton abstraction at $-31.0(-30.2)$ and $-31.8(-30.6)$ kcal/mol, respectively. The decomposition of these complexes leads to bihalide formation, $\text{SiH}_2 + \text{FHI}^-$ [$\Delta E_e(\Delta H_0) = 0.7(-1.0)$ kcal/mol], which can be considered athermic within the accuracy of our method. Bihalide formation was not investigated for $\text{CH}_3\text{I} + \text{F}^-$ in Ref. 24, meanwhile for $\text{SiH}_3\text{Cl} + \text{F}^-$, we observed the $\text{SiH}_2 + \text{FHCl}^-$ production as an endothermic reaction at higher collision energies with a low probability.⁴²

The hydride and iodide ions produced by the substitution reactions can also perform proton abstraction to form $\text{SiHFI}^- + \text{H}_2$ [$\Delta E_e(\Delta H_0) = -47.9(-51.0)$ kcal/mol] and $\text{SiH}_2\text{F}^- + \text{HI}$ [$\Delta E_e(\Delta H_0) = -7.2(-9.8)$ kcal/mol]. An exothermic three-fragment molecular hydrogen production channel, $\text{SiHF} + \text{H}_2 + \text{I}^-$ [$\Delta E_e(\Delta H_0) = -17.1(-20.3)$ kcal/mol], is also present, which can be formed by the decomposition of the dihydrogen-bond containing IDHBMIN [$-29.2(-29.1)$ kcal/mol] complex or the elimination of H_2 from SiH_3F following $\text{S}_{\text{N}}2$ (not depicted in Fig. 3). It is possible for the SiHF and I^- fragments to unite; therefore, the $\text{SiHFI}^- + \text{H}_2$ production has other mechanisms besides proton abstraction. It is even possible that WMIN and FSPostMIN complexes lose H_2 in a single step. The dihydrogen-bonded complex formation and the subsequent three-fragment molecular hydrogen production are characteristic of $\text{SiH}_3\text{Cl} + \text{F}^-$ as well. On the other hand, to our best knowledge, analogous complexes have never been observed in the case of carbon-centered ion-molecule reactions.

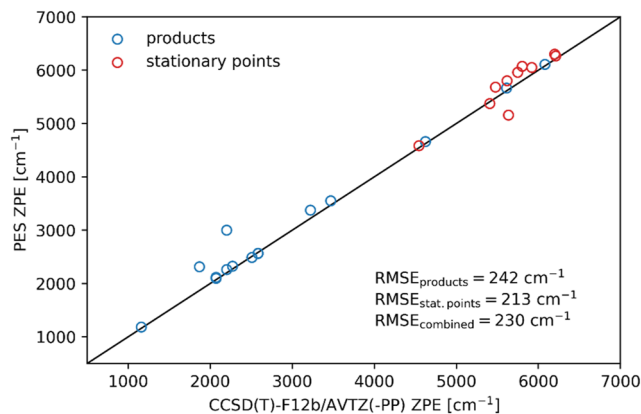


FIG. 4. Comparison of the values of the zero-point vibrational energies of stationary points in the interaction region and in the product channels as given by the fitted PES with those given by direct CCSD(T)-F12b/AVTZ(-PP) *ab initio* computations.

A highly endothermic three-fragment product formation, $\text{SiH}_2 + \text{HF} + \text{I}^-$ [$\Delta E_e(\Delta H_0) = 17.4(14.6)$ kcal/mol], is possible by the decomposition of the bihalide or the SiH_2I^- ion following the $\text{SiH}_2 + \text{FHI}^-$ production or proton abstraction, respectively. The analogous $\text{SiH}_2 + \text{HF} + \text{Cl}^-$ is observed in the case of the $\text{SiH}_3\text{Cl} + \text{F}^-$ system with even higher endothermicity.

Figure 3 also shows four stationary points that can be optimized on the PES with satisfactory accuracy but do not contribute to the most significant mechanisms: FDHBMIN at $-32.0(-30.9)$ kcal/mol, *syn*-IBHMIN at $-21.8(-22.6)$ kcal/mol, FDITS at $4.5(3.0)$ kcal/mol, and IDITS at $-7.8(-10.9)$ kcal/mol.

We chose not to include the $\text{SiH}_3 + \text{FI}^-$ channel in our schematic PES due to its extremely low probability, as only about a dozen $\text{SiH}_3 + \text{FI}^-$ formations were observed, only at the highest collision energy. Moreover, the fitted PES does not describe this region accurately due to electronic structure issues caused by the formation of two doublet product species.

A sufficiently accurate PES must reproduce the reaction energies of the product channels, and the zero-point energies of the stationary points must be realistic as well. Here, we seek to achieve chemical accuracy, which means errors below 1 kcal/mol (350 cm^{-1}). Figure 4 shows the correlation between the zero-point vibrational energies of the stationary points and the products obtained on PES506 and by direct coupled cluster theory. The RMSEs of the products and the stationary points are 242 and 213 cm^{-1} , and the combined RMSE is 230 cm^{-1} , which means the chemically accurate reproduction of the zero-point energies. According to Fig. 5, the RMSE of the classical reaction energies of the product channels is 0.19 kcal/mol, which is well within our target accuracy.

B. Reaction probabilities

Figure 6 shows the reaction probabilities as a function of the impact parameter of the various reactions calculated at different collision energies. The maximum reactive impact parameter decreases as the collision energy increases, as it is 26 and 10.5 bohrs at $E_{\text{coll}} = 1$ and 80 kcal/mol, respectively.

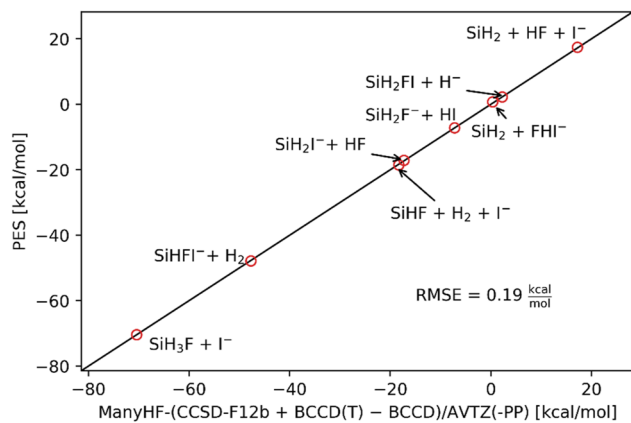


FIG. 5. Comparison of the classical reaction energies (without ZPE) of the product channels calculated on the fitted PES with the results obtained by the composite *ab initio* computations.

The total reactivity of the system is expressed as a sum of the opacity functions of the main and minor product channels, marked by the dashed gray line on the top row of Fig. 6. It reflects an extremely high reactivity at $E_{\text{coll}} = 1$ kcal/mol, as the $b = 0$ reaction probability is around 98%. Between $E_{\text{coll}} = 40$ and 80 kcal/mol, the total reaction probability decreases to 60% and 50%, respectively. The decrease in the overall reactivity indicates that the slow movement of the reactants is favorable, as they can attract each other

even from a distance. At higher collision energies, the significance of long-range attractive interactions diminishes.

The most significant contributions to the total reactivity are the iodide substitution and the proton abstraction. The combined reactivity of the system at $b = 0$, excluding these two product formations, marked by the magenta line, increases with the collision energy from 0.7% to around 3.7% at $E_{\text{coll}} = 1$ and 80 kcal/mol, respectively.

At $E_{\text{coll}} = 1$ kcal/mol, the probability of iodide substitution hovers around 70% within the range of $b = 0$ –10 bohrs. Between 10 and 22 bohrs, the probability decreases to ~40%, and beyond $b = 22$ bohrs up to b_{max} , it rapidly drops to zero. At $E_{\text{coll}} = 40$ and 80 kcal/mol, the opacity function for this reaction exhibits an approximately linear decrease between $b = 0$ and b_{max} .

We divided the opacity functions of the iodide substitution based on the stereochemistry of the SiH_3F product into inversion and retention, as depicted by Fig. 7. At $E_{\text{coll}} = 1$ kcal/mol, the probability of inversion hovers between 40% and 50% up to around $b = 20$ bohrs. Meanwhile, the retention channel exhibits a linearly decreasing opacity function. At higher collision energies, beyond $E_{\text{coll}} = 50$ kcal/mol, the inversion, retention, and combined opacity functions do not change significantly. In the applied collision energy range, both the maximum reactive impact parameter and the probability values at all impact parameters for inversion and retention decrease with increasing E_{coll} . The exception to this is the probability of retention between 1 and 5 kcal/mol at low and moderately high impact parameters, where the probability increases substantially.

For proton abstraction, the reaction probability at $b = 0$ is 29%, 6.6%, and 3.0% at $E_{\text{coll}} = 1$, 40, and 80 kcal/mol, respectively. The maximum probability is observed at higher impact parameters. At $E_{\text{coll}} = 1$ kcal/mol, the peak is only slightly higher than the $b = 0$ value,

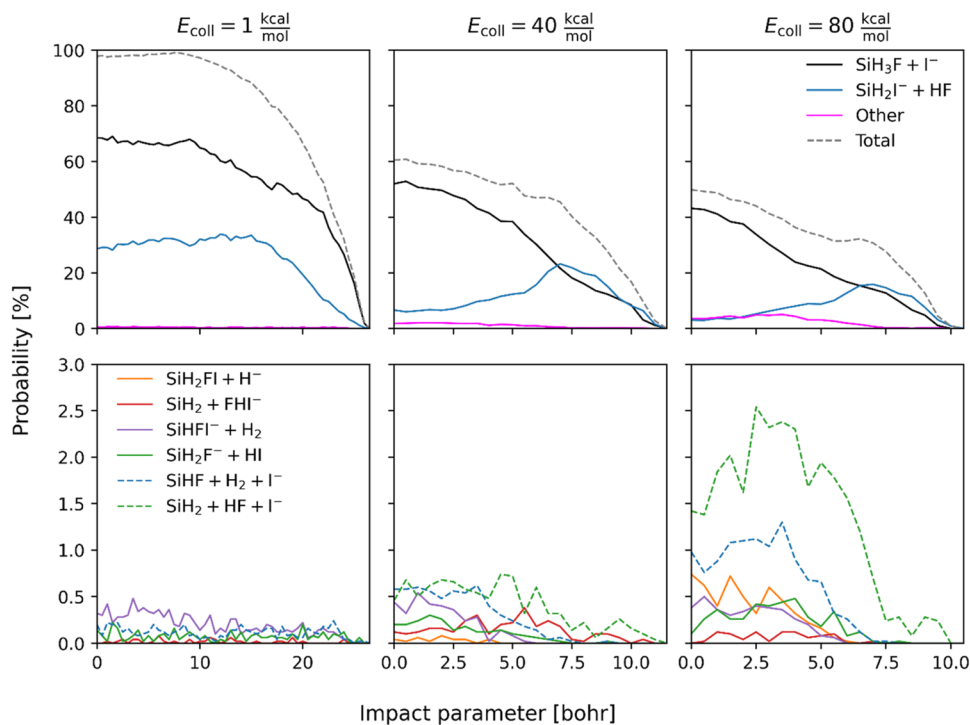


FIG. 6. Reaction probabilities of the product channels as a function of impact parameter obtained at 1, 40, and 80 kcal/mol collision energies. The upper panels show the opacity functions for the main channels and the sum of the contributions from minor channels (magenta line), and the lower panels show the probabilities for the minor product channels. The total reactivity means the sum of the probabilities of all product channels shown in the figure.

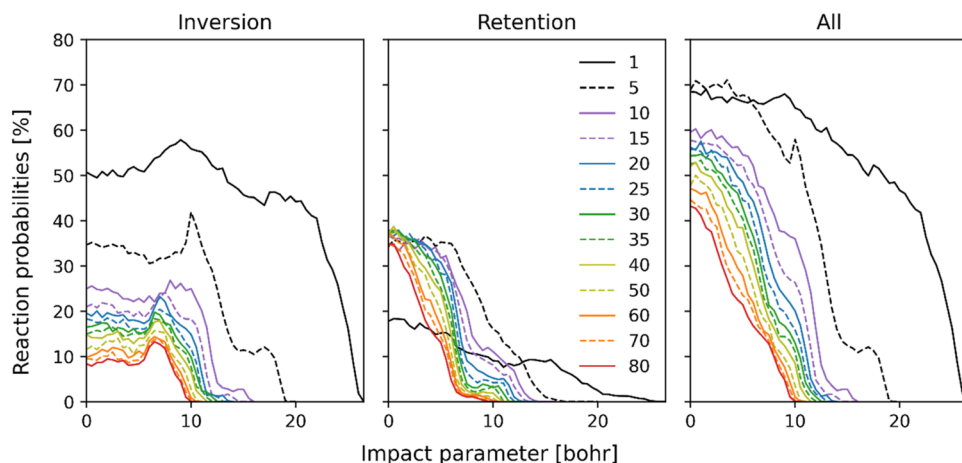


FIG. 7. Opacity functions of the iodide substitution leading to $\text{SiH}_3\text{F} + \text{I}^-$ divided into the contributions from inversion and retention at different collision energies (in kcal/mol).

reaching around 34%, which is observed at $b = 15$ bohrs. However, at higher collision energies, the opacity functions exhibit significantly higher peaks relative to the $b = 0$ reactivity, reaching 23% and 16% observed at $b = 7$ bohrs for both $E_{\text{coll}} = 40$ and 80 kcal/mol.

The $b = 0$ reaction probability of $\text{SiHFI}^- + \text{H}_2$ production hovers around 0.5%; meanwhile, its maximum reactive impact parameter decreases from 24.5 to 5.5 bohrs as the collision energy increases.

The formation of $\text{SiH}_2\text{F}^- + \text{HI}$ can be observed across the entire collision energy range, although with a low probability. At the lowest collision energy, it only reaches a few tenths of a percent over a wide range of impact parameters, up to b_{max} . At $E_{\text{coll}} = 40$ and 80 kcal/mol, the probabilities at $b = 0$ are somewhat higher, though still below 0.5%, and the maximum reactive impact parameter is reduced to 7.5 bohrs for this reaction.

The $\text{SiH}_2 + \text{FHI}^-$ reaction is observed throughout the entire collision energy range, primarily at medium collision energies, with reaction probabilities below 0.5%. This reaction is presumably not favoring the excessively high collision energy because the bihalide ion decomposes easily. It can also be a significant circumstance that the formation of the *anti*-FBHMIN or *syn*-FBHMIN complex preceding the formation of the bihalide is favored if the proton abstraction products move slowly.

In the case of hydride substitution, the probability at $b = 0$ increases at higher collision energies. It is nearly negligible at $E_{\text{coll}} = 40$ kcal/mol, but at $E_{\text{coll}} = 80$ kcal/mol, the probability at $b = 0$ reaches 0.7%.

The three-fragment molecular hydrogen production, $\text{SiHF} + \text{H}_2 + \text{I}^-$, is observed throughout the entire collision energy range with increasing $b = 0$ probability: 0.2%, 0.6%, and 1.0% at $E_{\text{coll}} = 1$, 40, and 80 kcal/mol, respectively.

The $\text{SiH}_2 + \text{HF} + \text{I}^-$ reaction is not observed at low collision energies. However, at the highest collision energy, this reaction becomes the third most significant, with around 1.4% probability at $b = 0$ and 2.5% at $b = 2.5$ bohrs.

C. Integral cross sections

Figure 8 presents the integral cross sections (ICSs) of the various reactions of the title system as a function of collision energy,

also known as the excitation function. These results are shown with soft, hard, and without vibrational energy constraints.

The excitation functions of the two most dominant reactions, iodide substitution [Fig. 8(a)] and proton abstraction [Fig. 8(b)], share a similar shape, characterized by a rapid, monotonic decrease with increasing collision energy.

In the case of iodide substitution [Fig. 8(a)], the ICS reaches 984 bohr² at the smallest collision energy of 1 kcal/mol, and at the highest collision energy, 80 kcal/mol, it decreases to 46 bohr². The excitation function of $\text{SiH}_3\text{F} + \text{I}^-$ is not affected by the zero-point vibrational energy constraint. Figure 9 shows this excitation function divided into inversion and retention channels. Inversion significantly dominates at low collision energies. As the collision energy increases, the difference in the ICSs decreases sharply. At $E_{\text{coll}} = 1$ kcal/mol, the contribution of the retention channel is 10%, while above 15 kcal/mol, it hovers around 45%.

The ICS for proton abstraction is 443 and 430 bohr² at $E_{\text{coll}} = 1$ kcal/mol, without and with the soft vibrational constraint, respectively [Fig. 8(b)]. When applying the hard vibrational constraint, the cross section at the lowest collision energy decreases to 224 bohr². At $E_{\text{coll}} = 80$ kcal/mol, the ICS is 30 bohr² in the unconstrained case and 24 bohr² using the hard constraint. The impact of the hard vibrational constraint on reducing the ICS becomes less significant as the collision energy increases.

The excitation function for $\text{SiH}_2\text{F}^- + \text{HI}$ formation exhibits a maximum at $E_{\text{coll}} = 1$ kcal/mol, reaching 1.45 bohr² without energy constraint, 1.26 bohr² with the soft vibrational constraint, and 0.28 bohr² with the hard vibrational constraint [Fig. 8(c)]. Between $E_{\text{coll}} = 5$ and 40 kcal/mol, the excitation function remains nearly flat. At higher collision energies, the cross section gradually increases with the collision energy, reaching 0.40 bohr² both with and without the soft energy constraint and 0.26 bohr² with the hard constraint.

In the case of $\text{SiHFI}^- + \text{H}_2$ production [Fig. 8(d)], the highest ICS is observed at the lowest collision energy at 3.08 bohr² both with soft and without energy constraint, and 1.51 bohr² with the hard constraint. The ICS rapidly decreases as collision energy increases. Between $E_{\text{coll}} = 10$ and 80 kcal/mol, the ICS stabilizes at around

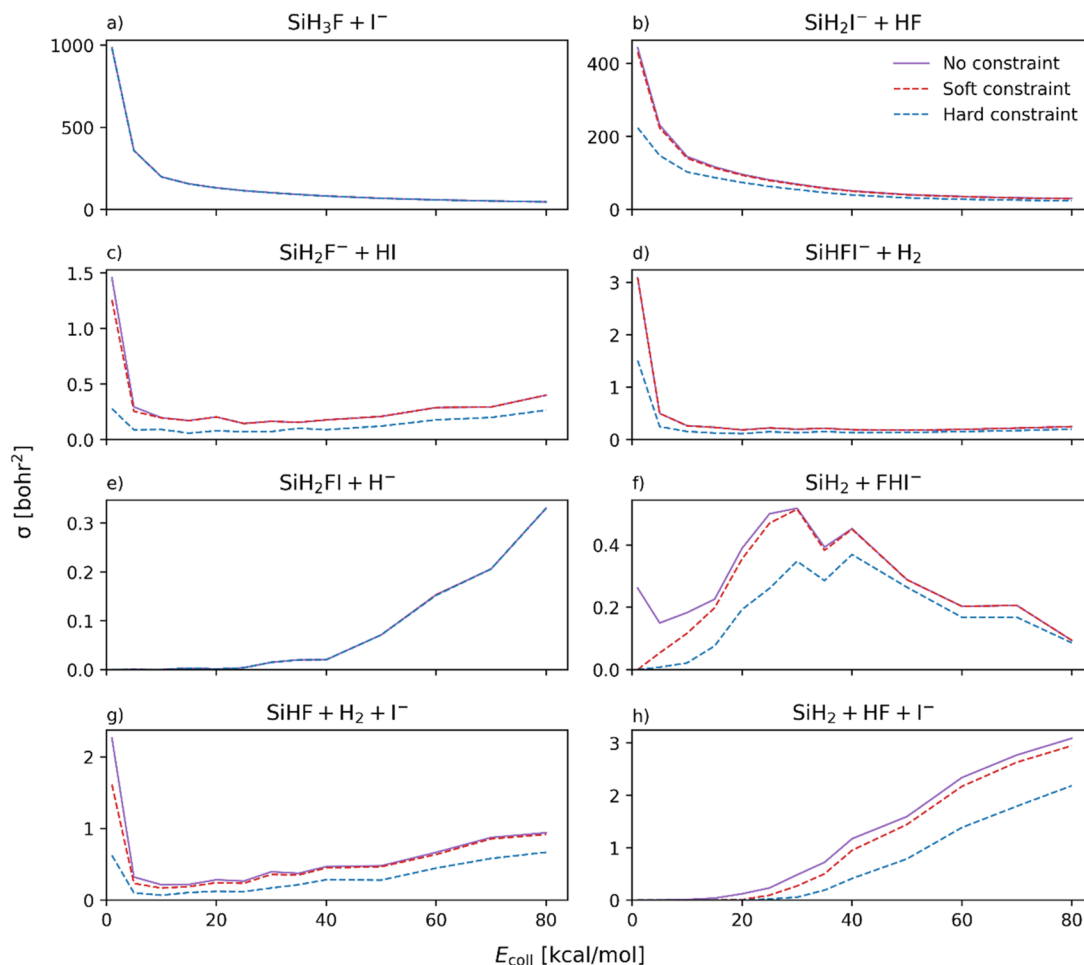


FIG. 8. Integral cross sections of the product channels as a function of collision energy with and without the soft and hard vibrational constraint.

0.2 bohr². Notably, the difference between the hard vibrationally constrained and the unconstrained functions becomes smaller as collision energy increases, and the soft constraint has no reducing effect at all.

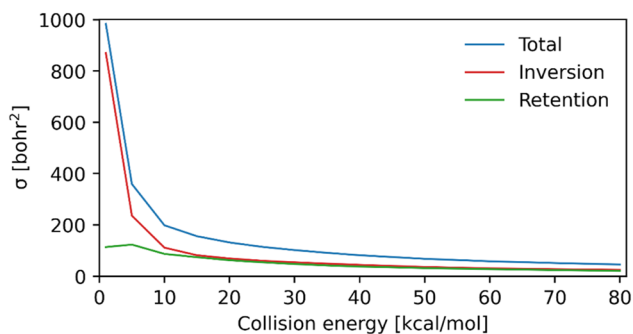


FIG. 9. Integral cross section of the iodide ion substitution divided into inversion and retention channels as a function of collision energy.

The excitation function of the hydride substitution channel [Fig. 8(e)] exhibits a distinct qualitative difference compared to the previously mentioned reactions. At collision energies below 20 kcal/mol, the cross section is zero, but beyond that, it steadily increases with the increasing collision energy. At $E_{\text{coll}} = 80$ kcal/mol, the ICS reaches 0.33 bohr². A noteworthy characteristic of the hydride substitution excitation function is that the influence of the vibrational constraint is negligible. There are no trajectories violating zero-point energy, even though it is not a particularly exothermic reaction.

The maximum ICS for the bialide production channel is observed at medium collision energies, at 30 kcal/mol, and it reaches 0.51 bohr² both with and without the soft vibrational constraint [Fig. 8(f)]. With the hard constraint, the ICS is 0.35 bohr² at this collision energy. At the highest collision energy, the ICS reduces to around 0.1 bohr², but the vibrational energy constraint has a minimal reducing effect. Conversely, at the lowest collision energy, the unconstrained ICS is 0.26 bohr², while the soft- and hard-constrained ICSs are zero.

The $\text{SiHF} + \text{H}_2 + \text{I}^-$ channel [Fig. 8(g)] has a similar ICS profile as that of the $\text{SiH}_2\text{F}^- + \text{HI}$ formation [Fig. 8(c)], characterized by a huge drop between 1 and 5 kcal/mol, from 2.26 to 0.32 bohr², followed by a slight increase at higher collision energies, reaching 0.94 bohr² at $E_{\text{coll}} = 80$ kcal/mol. The hard vibrational constraint reduces the cross sections to 0.62 and 0.67 bohr² at the smallest and highest collision energies.

The ICS of the $\text{SiH}_2 + \text{HF} + \text{I}^-$ reaction is negligible at the smallest collision energy but approximately linearly grows during its increase, reaching 3.09, 2.94, and 2.18 bohr² without, with soft, and with hard constraints at $E_{\text{coll}} = 80$ kcal/mol, respectively [Fig. 8(h)].

D. Reaction mechanisms

To gain a deeper understanding of the atomistic details of the mechanisms characteristic of the title system, we analyzed several trajectory animations of the most significant product formations at collision energies of 1, 20, 40, and 80 kcal/mol within the active impact parameter ranges. The coordinates of several representative trajectories are given in the [supplementary material](#).

The most significant product formation is the iodide substitution, resulting in the SiH_3F and I^- product pair. Typically, regardless of the initial orientation of the reactants at the beginning of the simulations, the initial step at the lowest collision energy is the formation of the Walden complex. Backscattering is characteristic for small impact parameters, while forward scattering predominates for higher impact parameters via the stripping mechanism. This preference for scattering angle persists at higher collision energies, where there is insufficient time for reactant reorientation, favoring the initial FSPostMIN formation.

At $E_{\text{coll}} = 1$ kcal/mol and low impact parameters, the most common initial step for proton abstraction is the formation of the WMIN complex, which subsequently decomposes by losing the fluoride ion and then abstracting a proton. At higher impact parameters, a more direct stripping mechanism dominates, lacking Si–F bond formation, resulting in forward scattering. It is common to observe complex formation in the exit channel of proton abstraction at low collision energy due to the slow movement of the separating fragments.

The most significant mechanism for the $\text{SiH}_2\text{F}^- + \text{HI}$ production is the iodide substitution followed by the proton abstraction by the leaving ion. Post-reaction IBHMIN formation frequently occurs, affecting the leaving direction. Low translational energy transfer may favor this mechanism for two reasons: first, the slower the departure of the iodide and SiH_3F coproducts of the $\text{S}_{\text{N}}2$ step, the greater the chance of the abstraction; second, due to the conservation of energy, less translational energy transferred results in more internal energy for SiH_3F , intensifying Si–H vibration. At the moderately high collision energy of 20 kcal/mol, we observed an interesting side reaction in which HI is formed in the decomposition of the IBHMIN complex originating from HF formation leading to bialide and the return of the bialide ion in the opposite orientation. At $E_{\text{coll}} = 40$ and 80 kcal/mol, we observed some instances of hydride substitution induced I^+ abstraction.

Hydride substitution is characteristic of higher collision energies. At $E_{\text{coll}} = 40$ kcal/mol, the FSPostMIN complex forms, releasing a hydride ion. At $E_{\text{coll}} = 80$ kcal/mol, hydride substitution follows a somewhat different route, with the initial step being the formation

of an Si–H–F bond, from which the hydride is expelled at the same time as the formation of the new Si–F bond.

The formation of $\text{SiHFI}^- + \text{H}_2$ proceeds through various mechanisms, each exhibiting different collision energy preferences. At the lowest collision energy of 1 kcal/mol, the primary mechanism involves the formation and decomposition of the dihydrogen-bonded IDHBMIN complex, followed by the subsequent reassociation of SiHF and I^- . Additionally, we observed a single-step H_2 elimination from the preceding WMIN or FSPostMIN complexes. Moreover, vibrationally excited SiH_3F can lose H_2 in a single step, and the SiHF fragment can combine with the iodide ion. At $E_{\text{coll}} = 20$ kcal/mol, the main mechanisms remain the decomposition of IDHBMIN and the direct one-step H_2 elimination from WMIN and FSPostMIN complexes, with the emergence of hydride ion proton abstraction. At even higher collision energies, hydride ion proton abstraction becomes the predominant mechanism for molecular hydrogen formation. Interestingly, the decomposition of the FDHBMIN dihydrogen-bonded complex, originating from HF, also occurs at the highest collision energies but in a minuscule proportion.

The bialide ion formation leading to $\text{SiH}_2 + \text{FHI}^-$ has a consistent mechanism across all collision energies: proton abstraction, FBHMIN complex formation, which decomposes by losing the bialide ion.

The three-fragment molecular hydrogen production, $\text{SiHF} + \text{H}_2 + \text{I}^-$, involves three main mechanisms: below $E_{\text{coll}} = 40$ kcal/mol, the predominant mechanism is the three-fragment decomposition of the IDHBMIN complex, while the single-step H_2 elimination from SiH_3F following $\text{S}_{\text{N}}2$ becomes more pronounced as the collision energy increases. Beyond $E_{\text{coll}} = 40$ kcal/mol, we observed the third mechanism, which involves molecular hydrogen production via the proton abstraction of the hydride and subsequent iodide ion elimination from the SiHFI^- co-product.

The $\text{SiH}_2 + \text{HF} + \text{I}^-$ reaction is characteristic of higher collision energies. At 20 kcal/mol, we observed that the main mechanism is the decomposition of FHI^- . At 40 kcal/mol, iodide ion elimination following proton abstraction is more common, along with HF elimination following $\text{S}_{\text{N}}2$. The latter two mechanisms are predominant at the highest collision energy, where bialide production is very rare.

IV. SUMMARY AND CONCLUSIONS

After conducting PES development and dynamics investigations for the $\text{F}^- + \text{SiH}_3\text{Cl}$ system, we extended our research to examine the analogous $\text{F}^- + \text{SiH}_3\text{I}$ gas-phase ion–molecule reactions using a similar methodology. We employed ROBOSURFER to automate the development process and utilized the Brueckner (T) term to obtain explicitly-correlated coupled-cluster singles, doubles, and perturbative triples level quality fitting sets. We utilized ManyHF in the *ab initio* calculations to reduce Hartree–Fock convergence issues. The fitting function is a full-dimensional sixth-order permutationally invariant polynomial with 10 810 coefficients expressed in terms of Morse variables, which represent exponentially transformed interatomic distances. For the fitting, we used a weighted least squares method. In contrast to our earlier $\text{F}^- + \text{SiH}_3\text{Cl}$ PES development, where we used a one-stage weighting

function [Eq. (2)], this time we utilized a more sophisticated three-stage weighting [Eq. (3)], which helped to avoid the high-energy but chemically relevant energy points contributing disproportionately less to the fitting.

During the development, we monitored the RMSE at chemically relevant PES regions, along with the ratio of unphysical trajectories. On the final PES, the ratio of unphysical trajectories is well below 1%, and the RMSE is ~ 1 kcal/mol, demonstrating that we achieved near chemical accuracy. Additionally, we compared the *ab initio* reaction energies of eight characteristic product channels to those of the PES-optimized ones, revealing an RMSE of 0.19 kcal/mol. Furthermore, we compared the ZPVEs of several optimized stationary points and products to the ZPVEs of the corresponding coupled cluster optimized vibrational energies, revealing chemically accurate agreement.

On our newly-developed PES, we conducted trajectory simulations within a collision energy range of 1–80 kcal/mol, uncovering a rich dynamics spectrum. This includes high-probability reactions such as S_N2 iodide ion substitution and proton abstraction, alongside lower-probability channels involving HI, H_2 , H^- , FHI^- , $HF + I^-$, and $H_2 + I^-$ formations. We divided the iodide ion substitution into inversion and retention channels and observed that both are significantly active in the entire collision energy range. S_N2 cross sections show that at low collision energy inversion dominates and at the highest collision energies “racemization” occurs.

Atomic-level mechanisms show a high degree of similarity between the title system and its chlorine analog, with some interesting differences. Comparing the present reaction to the carbon-centered cousin, we can conclude that the dynamics and mechanisms at silicon centers are much more complex.

SUPPLEMENTARY MATERIAL

See the [supplementary material](#) for Cartesian coordinates (\AA), absolute energies (E_h), and vibrational frequencies (cm^{-1}) of the stationary points corresponding to the fitted PES and the direct *ab initio* levels of $E_{\text{composite}}$ and CCSD(T)-F12b/AVTZ(-PP) for geometries and frequencies; reaction probabilities; integral cross sections; coordinates (\AA) along representative trajectories; as well as PES coefficients and codes (Ref. 52).

ACKNOWLEDGMENTS

We acknowledge the National Research, Development and Innovation Office—NKFIH, Grant No. K-146759; Project No. TKP2021-NVA-19, provided by the Ministry of Culture and Innovation of Hungary from the National Research, Development and Innovation Fund, financed under the TKP2021-NVA funding scheme; and the Momentum (Lendület) Program of the Hungarian Academy of Sciences for financial support.

AUTHOR DECLARATIONS

Conflict of Interest

The authors have no conflicts to disclose.

Author Contributions

Balázs J. Molnár: Data curation (lead); Formal analysis (lead); Investigation (lead); Methodology (equal); Software (equal); Visualization (lead); Writing – original draft (supporting); Writing – review & editing (supporting). **Attila Á. Dékány:** Data curation (supporting); Formal analysis (supporting); Investigation (supporting); Methodology (equal); Software (equal); Supervision (equal); Visualization (supporting); Writing – original draft (lead); Writing – review & editing (supporting). **Gábor Czakó:** Conceptualization (lead); Funding acquisition (lead); Project administration (lead); Supervision (equal); Writing – original draft (supporting); Writing – review & editing (lead).

DATA AVAILABILITY

The data that support the findings of this study are available within the [supplementary material](#) and from the corresponding author upon reasonable request.

REFERENCES

- 1 A. P. Bento, M. Solà, and F. M. Bickelhaupt, *J. Comput. Chem.* **26**, 1497 (2005).
- 2 A. P. Bento and F. M. Bickelhaupt, *J. Org. Chem.* **72**, 2201 (2007).
- 3 S. C. A. H. Pierrefixe, C. Fonseca Guerra, and F. M. Bickelhaupt, *Chem. - Eur. J.* **14**, 819 (2008).
- 4 M. A. van Bochove and F. M. Bickelhaupt, *Eur. J. Org. Chem.* **2008**, 649.
- 5 Z.-Z. Yang, Y.-L. Ding, and D.-X. Zhao, *J. Phys. Chem. A* **113**, 5432 (2009).
- 6 Y.-L. Ding, J.-R. Mu, and L.-D. Gong, *J. Chin. Chem. Soc.* **60**, 327 (2013).
- 7 M. V. J. Rocha, N. W. G. Smits, L. P. Wolters, A. de Cózar, C. Fonseca Guerra, T. C. Ramalho, and F. M. Bickelhaupt, *Int. J. Mass Spectrom.* **413**, 85 (2017).
- 8 T. Bettens, M. Alonso Giner, F. De Proft, T. A. Hamlin, and F. M. Bickelhaupt, *Chem. - Eur. J.* **26**, 3884 (2020).
- 9 T. H. Dunning, Jr., L. T. Xu, and J. V. K. Thompson, *J. Phys. Chem. A* **125**, 7414 (2021).
- 10 A. Á. Dékány, G. Z. Kovács, and G. Czakó, *J. Phys. Chem. A* **125**, 9645 (2021).
- 11 D. A. Tasi, Z. Fábrián, and G. Czakó, *Phys. Chem. Chem. Phys.* **21**, 7924 (2019).
- 12 D. C. Clary and J. Palma, *J. Chem. Phys.* **106**, 575 (1997).
- 13 H.-G. Yu and G. Nyman, *Chem. Phys. Lett.* **312**, 585 (1999).
- 14 P. Ayotte, J. Kim, J. A. Kelley, S. B. Nielsen, and M. A. Johnson, *J. Am. Chem. Soc.* **121**, 6950 (1999).
- 15 H. Tachikawa and M. Igarashi, *Chem. Phys. Lett.* **303**, 81 (1999).
- 16 L. A. Angel and K. M. Ervin, *J. Phys. Chem. A* **105**, 4042 (2001).
- 17 J. Mikosch, S. Trippel, C. Eichhorn, R. Otto, U. Lourderaj, J.-X. Zhang, W. L. Hase, M. Weidemüller, and R. Wester, *Science* **319**, 183 (2008).
- 18 C. Hennig and S. Schmatz, *Phys. Chem. Chem. Phys.* **14**, 12982 (2012).
- 19 J. Xie, R. Otto, J. Mikosch, J. Zhang, R. Wester, and W. L. Hase, *Acc. Chem. Res.* **47**, 2960 (2014).
- 20 I. Szabó and G. Czakó, *Nat. Commun.* **6**, 5972 (2015).
- 21 M. Stei, E. Carrascosa, M. A. Kainz, A. H. Kelkar, J. Meyer, I. Szabó, G. Czakó, and R. Wester, *Nat. Chem.* **8**, 151 (2016).
- 22 J. Xie and W. L. Hase, *Science* **352**, 32 (2016).
- 23 P. Liu, D. Wang, and Y. Xu, *Phys. Chem. Chem. Phys.* **18**, 31895 (2016).
- 24 B. Olasz, I. Szabó, and G. Czakó, *Chem. Sci.* **8**, 3164 (2017).
- 25 I. Szabó and G. Czakó, *J. Phys. Chem. A* **121**, 9005 (2017).
- 26 X. Ji, C. Zhao, and J. Xie, *Phys. Chem. Chem. Phys.* **23**, 6349 (2021).
- 27 J. Meyer, V. Tajti, E. Carrascosa, T. Györi, M. Stei, T. Michaelsen, B. Bastian, G. Czakó, and R. Wester, *Nat. Chem.* **13**, 977 (2021).
- 28 J. Qin, Y. Liu, and J. Li, *J. Chem. Phys.* **157**, 124301 (2022).
- 29 Y. Li, C. Li, D. Gao, and D. Wang, *J. Phys. Chem. A* **126**, 5527 (2022).

- ³⁰X. Lu, L. Li, X. Zhang, B. Fu, X. Xu, and D. H. Zhang, *J. Phys. Chem. Lett.* **13**, 5253 (2022).
- ³¹X. Lu, C. Shang, L. Li, R. Chen, B. Fu, X. Xu, and D. H. Zhang, *Nat. Commun.* **13**, 4427 (2022).
- ³²R. Wester, *Mass Spectrom. Rev.* **41**, 627 (2022).
- ³³S. Zhao, H. Wang, G. Fu, W. Zhen, M. Liu, L. Yang, and J. Zhang, *Precis. Chem.* **1**, 507 (2023).
- ³⁴X. Liu, S. Tian, B. Pang, H. Li, and Y. Wu, *Phys. Chem. Chem. Phys.* **25**, 14812 (2023).
- ³⁵A. Gutal and M. Paranjothy, *Phys. Chem. Chem. Phys.* **25**, 15015 (2023).
- ³⁶A. B. Nacsa, V. Tajti, and G. Czakó, *J. Chem. Phys.* **158**, 194306 (2023).
- ³⁷T. Gstir, T. Michaelsen, B. A. Long, A. B. Nacsa, A. Ayasli, D. Swaraj, F. Zappa, F. Trummer, S. G. Ard, N. S. Shuman, G. Czakó, A. A. Viggiano, and R. Wester, *Phys. Chem. Chem. Phys.* **25**, 18711 (2023).
- ³⁸S. Zhao, G. Fu, W. Zhen, H. Wang, L. Yang, and J. Zhang, *Phys. Chem. Chem. Phys.* **25**, 28086 (2023).
- ³⁹S. Rao and D. Wang, *Chin. J. Chem. Phys.* **36**, 169 (2023).
- ⁴⁰J. C. Lorquet, *J. Chem. Phys.* **159**, 094302 (2023).
- ⁴¹G. Czakó, B. Gruber, D. Papp, V. Tajti, D. A. Tasi, and C. Yin, *Phys. Chem. Chem. Phys.* **26**, 15818 (2024).
- ⁴²A. Á. Dékány and G. Czakó, *J. Chem. Phys.* **158**, 224303 (2023).
- ⁴³A. Á. Dékány and G. Czakó, *Phys. Chem. Chem. Phys.* **26**, 10008 (2024).
- ⁴⁴T. Györi and G. Czakó, *J. Chem. Theory Comput.* **16**, 51 (2020).
- ⁴⁵T. Györi and G. Czakó, *J. Chem. Phys.* **156**, 071101 (2022).
- ⁴⁶D. A. Tasi, T. Györi, and G. Czakó, *Phys. Chem. Chem. Phys.* **22**, 3775 (2020).
- ⁴⁷T. B. Adler, G. Knizia, and H.-J. Werner, *J. Chem. Phys.* **127**, 221106 (2007).
- ⁴⁸T. H. Dunning, Jr., *J. Chem. Phys.* **90**, 1007 (1989).
- ⁴⁹K. A. Peterson, D. Figgen, E. Goll, H. Stoll, and M. Dolg, *J. Chem. Phys.* **119**, 11113 (2003).
- ⁵⁰K. A. Brueckner, *Phys. Rev.* **96**, 508 (1954).
- ⁵¹H.-J. Werner, P. J. Knowles, G. Knizia, F. R. Manby, M. Schütz *et al.*, MOLPRO, version 2015.1, a package of ab initio programs, 2015, see <http://www.molpro.net>.
- ⁵²B. J. Braams and J. M. Bowman, *Int. Rev. Phys. Chem.* **28**, 577 (2009).
- ⁵³Z. Xie and J. M. Bowman, *J. Chem. Theory Comput.* **6**, 26 (2010).
- ⁵⁴J. M. Bowman, G. Czakó, and B. Fu, *Phys. Chem. Chem. Phys.* **13**, 8094 (2011).
- ⁵⁵T. Szűcs and G. Czakó, *J. Chem. Phys.* **159**, 134306 (2023).
- ⁵⁶B. Cordero, V. Gómez, A. E. Platero-Prats, M. Revés, J. Echeverría, E. Cremades, F. Barragán, and S. Alvarez, *Dalton Trans.* **2008**, 2832.
- ⁵⁷W. L. Hase, *Encyclopedia of Computational Chemistry* (Wiley, New York, 1998), pp. 399–407.
- ⁵⁸L. Verlet, *Phys. Rev.* **159**, 98 (1967).
- ⁵⁹W. C. Swope, H. C. Andersen, P. H. Berens, and K. R. Wilson, *J. Chem. Phys.* **76**, 637 (1982).
- ⁶⁰P. Papp, V. Tajti, and G. Czakó, *Chem. Phys. Lett.* **755**, 137780 (2020).
- ⁶¹D. Papp and G. Czakó, *Chem. Sci.* **12**, 5410 (2021).
- ⁶²V. Tajti, T. Györi, and G. Czakó, *J. Chem. Phys.* **155**, 124301 (2021).
- ⁶³D. A. Tasi and G. Czakó, *J. Chem. Phys.* **156**, 184306 (2022).
- ⁶⁴A. Giricz, G. Czakó, and D. Papp, *Chem. - Eur. J.* **29**, e202302113 (2023).
- ⁶⁵See https://gitlab.com/d_attila/qcta for the source code of the qcta (quasi-classical trajectory analyzer) Python package.
- ⁶⁶See https://d_attila.gitlab.io/qcta/index.html for the online documentation of qcta.